

Synergy of *in-situ* heterogeneous interphases tailored lithium deposition

Yinuo Li^{1,2,§}, Anjun Hu^{1,2,§} (✉), Xingdong Gan¹, Miao He², Jun Zhu² (✉), Wei Chen², Yin Hu^{1,2}, Tianyu Lei², Fei Li², Yaoyao Li², Yuxin Fan², Fan Wang^{1,2}, Mingjie Zhou^{1,2}, An Wen³, and Baihai Li^{1,3} (✉)

¹ School of Materials and Energy, University of Electronic Science and Technology of China, Chengdu 610054, China

² State Key Laboratory of Electronic Thin Film and Integrated Devices, University of Electronic Science and Technology of China, Chengdu 610054, China

³ Yangtze Delta Region Institute (Huzhou), University of Electronic Science and Technology of China, Huzhou 313001, China

[§] Yinuo Li and Anjun Hu contributed equally to this work.

© Tsinghua University Press 2022

Received: 29 June 2022 / Revised: 17 August 2022 / Accepted: 2 September 2022

ABSTRACT

The implementation of a robust artificial solid electrolyte interphase (ASEI) to replace the unstable natural SEI can regulate lithium deposition behaviors and avoid the safety hazards caused by dendrites permeation in lithium metal batteries. Despite of devoted efforts in tailoring components of ASEI, the intrinsic mechanism of interfacial synergy within the heterogeneous interphases has not been well elucidated yet. Herein, we show that the lithium plating/stripping behaviors can be substantially enhanced (over 900 h with an overpotential of less than 20 mV at 1 mA·cm⁻² in Li|Li symmetric cells and 146 cycles in anode-free cells) by regulating the heterogeneous interphases. This favorable ASEI composed of LiF and Li₃N components can be *in-situ* generated during cycling by large-scale fabricated fluorinated boron nitride coatings. Further, the synergy of each heterogeneous component within ASEI was explored theoretically and experimentally. Li₃N has high adsorption energy and low ion diffusion barrier, which facilitates the transport of lithium ions and avoids its local accumulation to evolve into dendrites. Both the substrate and LiF are interfacially stable with high electron tunneling barriers, preventing the electrolyte decomposition and parasitic reactions. Finally, the high stiffness of the boron nitride also ensures lithium dendrites are suppressed once they grow, providing a stable environment for long-term cycling of lithium metal batteries.

KEYWORDS

in-situ heterogeneous solid electrolyte interphase (SEI), lithium deposition, dendrite-free, first-principles calculations

1 Introduction

The energy density limitation (~ 300 Wh·kg⁻¹) of lithium-ion batteries based on intercalation chemistry creates a bottleneck for the energy storage devices [1, 2]. Scientists have turned their attention to lithium (Li) metal anodes due to its high theoretical capacity (3,860 mAh·g⁻¹) and the lowest reduction potential (-3.04 V vs. standard hydrogen electrode) [2–5]. As a result of the high reactivity of Li, a solid electrolyte interphase (SEI) is spontaneously formed on Li metal anode when encountering with the electrolyte. Unfortunately, the natural SEI is too fragile to withstand the volume changes during Li plating and stripping. During cycling, the natural SEI will suffer the repeated fragmentation and reconstruction, exhibiting inhomogeneities in morphology and ionic conductivity [6]. Induced by the tip effect, the Li⁺ flux reaches the electrode surface unevenly for deposition, and dendrites gradually evolve where Li accumulates [7, 8]. Eventually, the unrestrained dendrites will permeate the separator, resulting in short-circuit risk. In addition, high electronic conductivity of natural SEI usually triggers parasitic reactions at the electrode–electrolyte interface and accelerates the electrolyte consumption [9, 10], failing to provide a stable environment for Li

plating and stripping. Therefore, it is urgent to find a designable and controllable SEI, which should satisfy the following requirements: (i) homogeneous chemical components with ion modulation capability, electrochemically avoiding Li dendrite formation; (ii) low electron conductivity to prevent side reactions and electrolyte depletion; and (iii) high mechanical strength to accommodate the volume expansion caused by Li plating/stripping, physically inhibiting dendrite growth.

These physical and chemical properties of the SEI are predominantly governed by its components and structure [11–13]. It has been confirmed that the SEI consists of outer organic layers and inner inorganic layers (e.g., LiF, Li₂CO₃, Li₂O, and Li₃N) [14]. Among these, LiF is favored due to its high interfacial energy towards Li and low electronic conductivity, and numerous efforts have been devoted to construct various LiF-rich SEIs [15–18]. Although the increased proportion of LiF in SEI can stabilize the electrode/electrolyte interface and inhibit the growth of dendrites to a certain extent, the regulation effect is limited due to inherently poor ionic conductivity of LiF. Among the typical SEI compositions, Li₃N has been reported to produce superior ion conductivity (ionic conductivity: 10⁻³ to 10⁻⁴ S·cm⁻¹, room temperature) and high stability toward Li metal [19–22].

Address correspondence to Anjun Hu, anjunhu_uestc@163.com; Jun Zhu, junzhu@uestc.edu.cn; Baihai Li, libaihai@uestc.edu.cn

Therefore, Li_3N is expected to provide a fast channel for Li^+ transport, preventing Li accumulation to evolve into dendrites. However, Li_3N has the disadvantages of the low interfacial energy against metallic Li and a narrow band gap [11, 23], resulting in a poor inhibition ability of Li_3N against dendritic growth. It is foreseeable that the effect of applying single Li_3N component as the artificial SEI (ASEI) regulator will not be prominent. In order to approach the optimal effect of SEI, the synergy of heterogeneous components is required. Recent studies have achieved favorable results by constructing hybrid ASEIs such as $\text{Li}_3\text{Sb}/\text{LiF}$ [6] and $\text{Li}_3\text{PO}_4/\text{Li}_3\text{N}$ [24] at the anodic interface. In this contribution, we combine the merits of the two typical components of LiF and Li_3N . It can be expected that these two beneficial components could synergistically regulate Li deposition behavior, which, however, has not been realized so far.

Herein, a favorable ASEI was constructed by incorporating large-scale fluorinated boron nitride (F-BN), where heterogeneous LiF and Li_3N components were *in-situ* generated during cycling, to elucidate the synergistic mechanism of the components on Li deposition behaviors. Under the synergistic effects of the components in heterogeneous interphases, the extended cycle life in Li|Li symmetric cells (900 h) and anode-free full cells (146 cycles) can be achieved. Furthermore, we explored the contributions of each heterogeneous component in ASEI through theoretical calculations and experimental evidences. The fluorinated substrate can stabilize Li metal and form stable chemical bonds with it to construct SEI layers containing Li_3N and LiF. Among them, Li_3N with low ion diffusion barrier accelerates Li^+ transport, giving rise to the uniform ion flux on electrode surface and resultant dense Li deposition. The high interfacial energy of LiF suppresses dendrite growth while the large electron tunneling barrier stabilizes Li plating/stripping. This work contributes to exploit the synergistic effects of the beneficial components in the artificial interphases for constructing dendrite-free Li metal batteries.

2 Experimental

2.1 Electrode preparation

To obtain F-BN, hexagonal boron nitride (h-BN, 99.9%, ≤ 50 nm), and fluoroboric acid (HBF_4 , AR, $> 40.0\%$) were sufficiently reacted at 50°C for 12 h, followed by washing and drying process. F-BN/h-BN and polyvinylidene fluoride (PVDF) binder were dispersed in N-methyl pyrrolidone (NMP, AR, $> 99.0\%$) solvent with a ratio of 9:1. The well-mixed slurry was uniformly spread on the Cu foil with a blade. After blast drying for several hours, F-BN/h-BN coated current collectors were prepared. The thickness of the coating was controlled by the spacing of the blade. The Li foil surface was cleaned by tetrahydrofuran (THF, $\geq 99.5\%$) before use. Cathodes in anode-free full cells were prepared by coating the Li_2S slurry on to the carbon-coated aluminum foil. The Li_2S slurry was uniformly mixed by Li_2S , acetylene black, and PVDF in a ratio of 7:3:1.

2.2 Characterization

X-ray diffraction (XRD) pattern was performed on Rigaku Ultima IV, Cu $K\alpha$ ($\lambda = 1.5406$ Å) radiation. Morphological characterization and elemental distribution were carried out on a scanning electron microscope (SEM, FEI NANOSEI 450), transmission electron microscope (TEM) equipped with X-ray energy dispersive spectrometer (EDS). *In-situ* light microscopy was used to detect Li deposition behavior in real time. X-ray photoelectron spectroscopy (XPS) was studied using Thermo Scientific K-Alpha⁺ with monochromatic Al $K\alpha$ radiation

(1,486.6 eV). Contact angles were observed by the OCA20 system. Electronic conductivity was given by ST2722-SD with ST2643 high resistance equipment using four-terminal method.

2.3 Electrochemical measurements

All cells were assembled in the argon-filled glove box, with water oxygen content below 0.1 ppm, of which Li|Li symmetric cells used CR-2032 type coin, and Li|Cu half-cells and anode-free anode full cells used CR-2025 type coin cells for testing. The electrolyte consisted of 1 M lithium bis (trifluoromethane) sulfonimide salt (LiTFSI) with 2% LiNO_3 dissolved in 1,3-dioxolane (DOL) and 1,2-dimethoxyethan (DME) (1:1, v/v), 40 μL per cell. Polypropylene (PP, Celgard 2400) was used as the separator. The constant current cycling of the cell was carried out on a LAND CT2001A at room temperature. The anode-free full cells were operated between 1.7–2.7 V vs. Li/Li⁺ after the first charge to 3.7 V. The electrochemical impedance spectroscopy (EIS) was studied using CHI 660E. The alternating current (AC) signal amplitude was 5 mV and the frequency was between 0.1 and 100 kHz when measured. The current–time curves used for the measurement of ion transfer number were also completed on CHI 660E.

2.4 Computation

All the first-principles computations based on generalized density function theory (DFT) were performed by Vienna *ab initio* simulation (VASP) software package [25]. The Perdew–Burke–Ernzerh generalized gradient approximation (GGA-PBE) [26] and the projector augmented wave (PAW) [27] pseudopotentials were employed to describe the exchange–correlation energy and the electron–ion interactions, respectively. The cutoff energies were set to be 450 eV and the Brillouin zone grid k -point spacing was 0.01 Å⁻¹. The atomic force configuration optimization convergence criterion was 0.01 eV·Å⁻¹. Climbing-image nudged elastic band (CI-NEB) method [28] in VASP was used to determine the kinetic diffusion barrier of lithium atom. More details information can be found in S1 in the electronic supplementary material (ESM).

3 Results and discussion

3.1 Construction and characterization of the ASEI

h-BN was first fluorinated by HBF_4 through ionic bonding [29], which was uniformly mixed with NMP solvent and PVDF binder to prepare slurry. The homogeneous slurry was cast onto Cu foil and uniformly spread with a blade, which can be large-scale fabricated (Figs. 1(a) and 1(b)). The thickness of coating controlled by blade's parameter was measured on the cross-sectional SEM, e.g., 50 μm -spacing blade corresponds the coating with a thickness of 7.9 μm (Fig. 1(c)). The surface morphology and thickness of other controllable coatings are presented in Fig. S1 in the ESM. The XRD patterns (Fig. S2 in the ESM) indicate that the fluorination process maintains the lattice structure of h-BN. TEM images reveal more information about the F-BN (Fig. S3 in the ESM). As presented in the high-resolution TEM (HRTEM) in Fig. 1(d), the distance between two adjacent fringes of the (110) and (002) crystal planes are 0.217 and 0.333 nm, respectively, which is consistent with the XRD results. As shown in Fig. S4 in the ESM, the EDS mapping illustrates that the fluorine elemental is uniformly distributed on the F-BN nanosheets. The chemical state of each element in F-BN can be analyzed from the XPS in Figs. 1(e)–1(g) and Fig. S5 in the ESM. Two peaks at 190.2 and 191.3 eV were observed in the fine spectra of B 1s, which originate from the B–N bond and B–F bond, respectively. The doped F

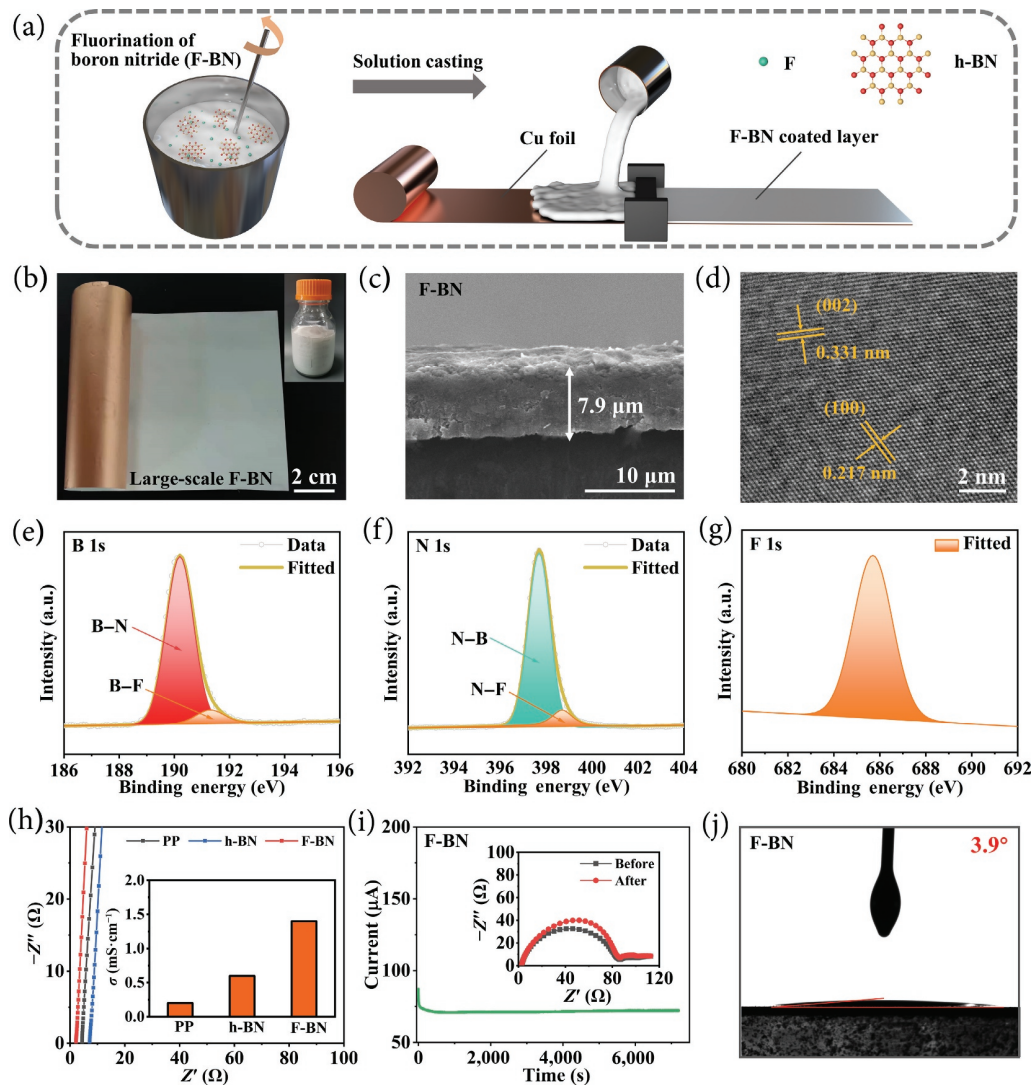


Figure 1 Construction and characterization of the interphase. (a) Schematic diagram and (b) digital photographs of large-scale coatings. (c) Thickness measurement on the cross-section SEM image of F-BN coating. (d) HRTEM image of fluorinated boron nitride corresponding to the yellow circle in Fig. S3 in the ESM. (e) and (f) XPS spectra of B 1s, N 1s, and F 1s of fluorinated boron nitride. (h) Ionic conductivity of PP separator, h-BN coating, and F-BN coating. (i) Current–time plots of the Li|Li symmetrical cell with F-BN after application of a constant potential (10 mV) and EIS variation before and after polarization. (j) The contact angle measurement of F-BN coating.

atoms also form bonds with N atoms, which can be verified in the N 1s spectra. The peak at 398.7 eV is attributed to N–F bond, and the other peak at 397.7 eV is assigned to the N–B bond, which is consistent with the previous reports [30, 31]. The peak of F 1s is located at 685.7 eV further confirms that F atoms are successfully grafted onto h-BN via the formation of stable chemical bonding.

In addition to the above characterizations, we also discovered some excellent physical properties of F-BN as ASEI to be applied to lithium metal batteries. On one hand, high ionic conductivity and ion transfer number can accelerate the Li^+ transport through ASEI, which is beneficial for uniform and dense Li plating [32, 33]. On the other hand, the superior electronic insulative properties can block electrons from tunneling through ASEI and prevent electrolyte decomposition [34, 35]. After fluorination, the ionic conductivity increases from 0.6×10^{-3} for h-BN to $1.4 \times 10^{-3} \text{ S}\cdot\text{cm}^{-1}$ for F-BN (Fig. 1(h)), and the ion transfer number increases from 0.3 to 0.73 (Fig. 1(i) and Fig. S6 in the ESM). Meanwhile, the electronic conductivity of F-BN ASEI was measured to be $2.3 \times 10^{-7} \text{ S}\cdot\text{cm}^{-1}$, inheriting the features of h-BN as a typically highly insulating material. Besides, the contact angle of the F-BN ASEI was measured to be 3.9° (Fig. 1(j)) while h-BN ASEI and bare Cu show larger contact angles of 4.2° and 23.1° (Fig. S7 in the ESM), respectively. This high electrolyte wettability of F-BN ASEI is

favorable for the formation of a stable electrode/electrolyte interphase and facilitates fast ion transport [36].

3.2 Evaluation of the Li plating/stripping stability

Li|Cu half cells, Li|Li symmetric cells, and anode-free full cells were assembled to explore the stability of Li plating/stripping regulated by F-BN ASEI. First, the ASEI with different thickness was investigated in Li|Cu cells at a current density of $1 \text{ mA}\cdot\text{cm}^{-2}$ with a capacity of $1 \text{ mAh}\cdot\text{cm}^{-2}$ and the corresponding Coulombic efficiency (CE) is shown in Fig. 2(a). The F-BN ASEI with optimized thickness of $7.9 \mu\text{m}$ exhibits the superior cycle performance for more than 150 cycles with a stable CE remains above 97%. In contrast, the h-BN and bare Cu can only operate for 70 and 120 cycles before the huge fluctuation of CE (Fig. 2(b)). The corresponding galvanostatic voltage profiles are presented in Fig. S8 in the ESM to further investigate the process of Li plating and stripping. As shown in Fig. S8(a) in the EMS, compared with the initial nucleation overpotential (μ_{nuc}) of bare Cu (54 mV) and h-BN (31 mV), the μ_{nuc} of F-BN (19 mV) is notably reduced. This result indicates that the nucleation barrier of F-BN ASEI is lower during Li deposition. Voltage profiles of Li plating/stripping at 10th cycle are given in Fig. S8(b) in the ESM. The Li|F-BN@Cu half cell shows the lowest voltage hysteresis between plating and

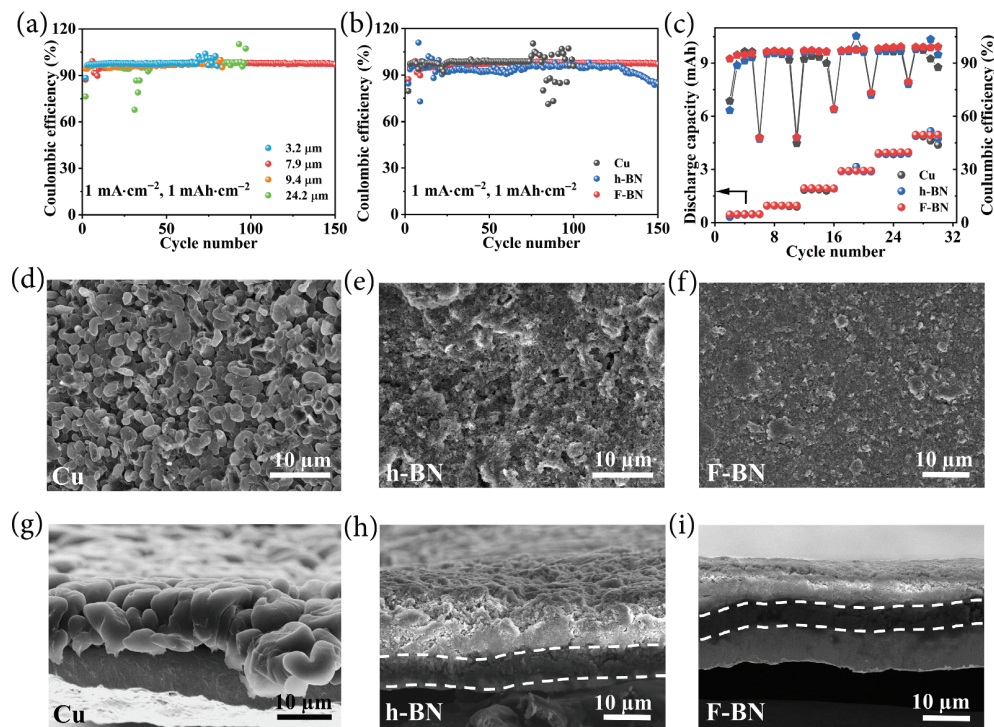


Figure 2 Electrochemical performance in Li||Cu cells and deposition morphology of Li. Long cycle stability of Li||Cu cells with different thickness F-BN ASEI (a) and bare Cu, h-BN ASEI (b). (c) Rate performance of Li||Cu cells with bare Cu, h-BN ASEI, and F-BN ASEI, the Li plating/stripping capacity gradually increases from 0.5 to 5 mAh·cm⁻² with a current density of 1 mA·cm⁻². The top surface (d)–(f) and cross-section (g)–(i) SEM images after Li deposition with bare Cu, h-BN ASEI, and F-BN ASEI.

stripping. In addition, the Li||F-BN@Cu half cell achieves a higher stripping capacity compared with controlled groups, which is consistent with the high CE in Fig. 2(b). Moreover, the voltage hysteresis and stripping voltage curve remain stable during following cycling, as shown in Fig. S8(c) in the ESM. Therefore, the electrode reversibility of Li plating/stripping can be significantly improved by the interfacial modulation of F-BN ASEI.

In the subsequent investigation, the 7.9 μm-thickness F-BN ASEI was used as the experimental group to provide comparison. The rate performance of Li||Cu half-cells was carried out with a fixed current density of 1 mA·cm⁻² to stepwise increase the Li plating/stripping capacity from 0.5 to 5 mAh·cm⁻², and the results are presented in Fig. 2(c). Even at high plating capacity up to 5 mAh·cm⁻², F-BN remains the excellent ability of completely stripping while h-BN and bare Cu exposes instability of CE. The results demonstrate the excellent rate behavior of F-BN ASEI.

To investigate the role of F-BN ASEI during Li plating and stripping, the electrodes at different states were taken out and observed by SEM analysis (Figs. 2(d)–2(i)). After initial Li plating, incompact-stack and randomly-oriented whisker-like Li deposition can be observed on the surface of bare Cu. Whereas the surface of h-BN and F-BN is flat and dense, where close-aligned Li is deposited underneath the coating (Fig. S9 in the ESM). For the case of Li depositing directly on bare Cu, dead Li accumulates after 10 cycles (Fig. S10 in the ESM), which cannot effectively participate in subsequent cycles. In comparison, the h-BN and F-BN coatings are still in close contact with the deposited Li layer. The *in-situ* optical microscopy was further employed to visualize the dynamic Li deposition process on bare Cu and F-BN ASEI. As shown in Fig. S11 in the ESM, the Li plated on bare Cu was as fluffy as foam, there were obvious protrusions in a short time and they evolve into dendrites almost instantly. Meanwhile, not only the electrode surface under the F-BN ASEI was still smooth and flat, but also the Li plating layer remained dense, which is consistent with the stage detection by SEM result. These results imply that the natural SEI on bare Cu is very fragile, dead Li and

dendrites tend to propagate on the electrode surface during plating and stripping, while the ASEI produced by the highly insulative and mechanically strong F-BN can hinder the electron tunneling while physically flatten the protrusions to suppress dendrite growth. Especially, F-BN ASEI has a more favorable effect on regulating the Li deposition behaviors. Li||Li symmetric cells were evaluated at a current density of 1 mA·cm⁻² with a capacity of 1 mAh·cm⁻² (Fig. 3(a)). The Li||Li symmetric cell with bare Cu suffers from a large polarization where the hysteresis voltage increases rapidly from 50 mV to several hundred millivolts after 700 h. As for that with h-BN ASEI, although the hysteresis voltage is low at initial stage, a short circuit occurs after 200 h. In contrast, the cell with F-BN ASEI can maintain a stable cycle of 900 h with a low overpotential of less than 20 mV. Moreover, the performance comparison under variable current density (0.5 to 5 mA·cm⁻²) is shown in Fig. 3(b). The overpotential of h-BN and F-BN did not exceed 50 mV at maximum, the overpotential of F-BN is slightly smaller and has almost no fluctuation. Whereas the overpotential of bare Cu fluctuates significantly with increasing current densities, and reaches to about 130 mV at 5 mA·cm⁻², which exhibits instability at the same current density. The low overpotential during the cycling and rate tests indicates the low impedance of the F-BN ASEI, which can be demonstrated by EIS test at different stages (Fig. S12 in the ESM). The impedances of artificial SEI are lower than those of natural SEI impedance of bare Cu in different stages, reflecting the fast Li⁺ transport properties at the electrode/electrolyte interface and even distribution of Li⁺ flux.

Minimizing the lithium dosage to zero excess to form the anode-free configuration, the Li plating and stripping behaviors of the full cell were further investigated under realistic condition [37–41]. In general, the cathode is constructed from a Li-rich material, while the anode is served by a lithium-free current collector. During the first charging process of the battery, the Li⁺ deintercalated or disintegrated from the cathode are reduced to metallic Li on the current collector. In the subsequent cycling, the anode-free cell operates in the same manner as traditional lithium metal batteries.

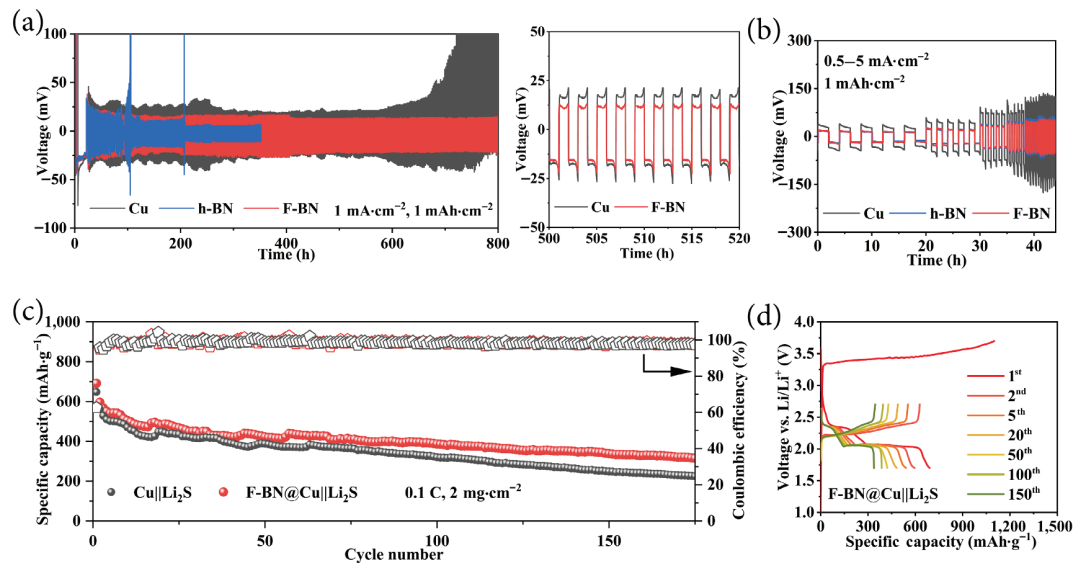


Figure 3 Electrochemical performance in Li|Li symmetric cells and anode-free full cells. (a) Voltage profiles of Li|Li symmetric cells with bare Cu, h-BN ASEI, and F-BN ASEI at $1 \text{ mA}\cdot\text{cm}^{-2}$ for $1 \text{ mAh}\cdot\text{cm}^{-2}$. (b) Rate performance tests at various current densities from 0.5 to $5 \text{ mA}\cdot\text{cm}^{-2}$ with a fixed capacity of $1 \text{ mAh}\cdot\text{cm}^{-2}$. Long-term cycling performance (c) and charge/discharge curves (d) of the F-BN@Cu||Li₂S full cell at 0.1 C, the loading of the cathodes is $2 \text{ mg}\cdot\text{cm}^{-2}$.

In our work, Li₂S with high theoretical capacity ($1,166 \text{ mAh}\cdot\text{g}^{-1}$) [42, 43] was employed as the cathode and bare/coated Cu as the current collectors. The XRD pattern (Fig. S13 in the ESM) as well as the SEM images and the corresponding element distribution mapping (Fig. S13 in the ESM) of the cathode imply that Li₂S are homogeneously mixed. The Li plating and stripping behaviors of the anode-free full cells are investigated in Fig. 3(c). After Li₂S being successfully activated (Fig. 3(d)), the F-BN@Cu||Li₂S full cells with Li₂S loading of $2 \text{ mg}\cdot\text{cm}^{-2}$ provide a higher initial discharge capacity of $691 \text{ mAh}\cdot\text{g}^{-1}$ at 0.1 C, and still maintain a discharge capacity of $346 \text{ mAh}\cdot\text{g}^{-1}$ (50% of capacity retention) after 146 cycles. However, the reversible capacity of Cu||Li₂S dropped to 50% of the initial capacity after 99 cycles, and the capacity retention was only 39% after 146 cycles. These results indicate that the *in-situ* F-BN ASEI can effectively improve the stability of Li plating/stripping.

3.3 Synergy mechanism of heterogeneous interphases

Encouraged by the superior Li plating/stripping stability and excellent cycle performance of F-BN ASEI, the underlying mechanism was further explored. The surface composition of F-BN ASEI (Figs. S15(a) and S15(b) in the ESM) and h-BN ASEI (Figs. S15(c)–S15(e) in the ESM) after 10 cycles was analyzed by XPS spectra. In the B 1s spectra of F-BN ASEI after lithiation, only B–N peak at 190.9 eV can be observed. For the chemical environment of N 1s, in addition to the peak at 397.9 eV corresponding N–B, the Li₃N peak at 398.5 eV was also found. Compared with the N 1s spectra before cycling (Fig. 1(f)), the N–F peak almost disappeared due to fact that the less electronegativity Li requires lower energy when competing with N for F. Considering the F 1s spectrum, LiF (685.1 eV) and –CF₃ (688 eV) can be detected during cycling. In h-BN SEI, Li₃N was also observed in N 1s spectra. After the XPS results being dissected, we further systematically and deeply investigated the synergy interactions of heterogeneous interphases by means of theoretical calculations.

DFT calculations were carried out to elaborate the role of the F-BN ASEI on Li deposition behaviors. A basic h-BN hexagonal lattice was constructed with a B–N bond length of 1.45 Å after structural optimization, and four possible fluorine atomic positions (B-top, N-top, bridge, and hollow) on the h-BN monolayer were considered to construct the atomic model of F-

BN (Fig. S16(a) in the ESM). As summarized in Fig. 4(a), the B-top was identified as the stable adsorption site on the h-BN with the maximum adsorption energy (1.60 eV) for the F atom. The XPS spectra suggested that h-BN generated ASEI contains Li₃N, and F-BN generated ASEI contains both Li₃N and LiF. SEM images indicating the subsequent metallic Li will be continuously deposited underneath these two ASEIs. Therefore, the interaction between Li and these four substrates (h-BN, F-BN, Li₃N, and LiF) needs to be fully discussed. Firstly, the adsorption behaviors of Li on these four substrates were investigated. Among the four candidate sites of h-BN, the hollow site with an adsorption energy of 0.096 eV was determined as the most stable site for Li. Six possible adsorption sites on F-BN are given in Fig. 4(b). After geometric optimization, Li moved to the pseudo-hollow (p-hollow) position, which is deviated from the perfect center of the six-atom B–N ring, yielding the maximum adsorption energy of 4.78 eV. The fluorination was demonstrated to significantly enhance the lithophilicity of BN, resulting in the lower nucleation barrier of Li and the weaker polarization [44]. For the Li₃N and LiF components in ASEI, three adsorption sites (Figs. S16(b) and S16(c) in the ESM) were considered, respectively. On the Li₃N (001) surface, the hollow site generated the strongest adsorption energy for Li, which was calculated to be 2.29 eV. The F-top site on the LiF (001) surface has the largest Li adsorption energy (0.67 eV). Therefore, Li₃N component exhibits the stronger lithophilicity than that of LiF.

The Li-ion diffusion behavior was investigated between the stable adsorption sites of the matrix and the results are presented in Figs. 4(c)–4(f). Li-ion diffuses between the hollow sites on h-BN with Li-ion on the B–N bridge as an intermediate state, and the energy barrier to be overcome is 0.04 eV. On the F-BN surface, there are two possible diffusion paths. Path-I means that Li-ion diffuses between the p-hollow sites with the nearest hollow site of the reference F atom as the transition state, overcoming the energy barrier of 0.68 eV. In Path-II, Li-ion directly follows the curve around the F atom to reach another stable adsorption site with a diffusion energy barrier of 0.38 eV. The F-BN exhibits both larger adsorption energy and diffusion barrier for lithium, that is, lithium tends to be anchored on the surface of F-BN at initial stage of deposition, which is beneficial for lithium to form chemical bonds on the surface to build a strong ASEI instead of weaker van der Waals forces. In the subsequent cycling, a lower diffusion energy

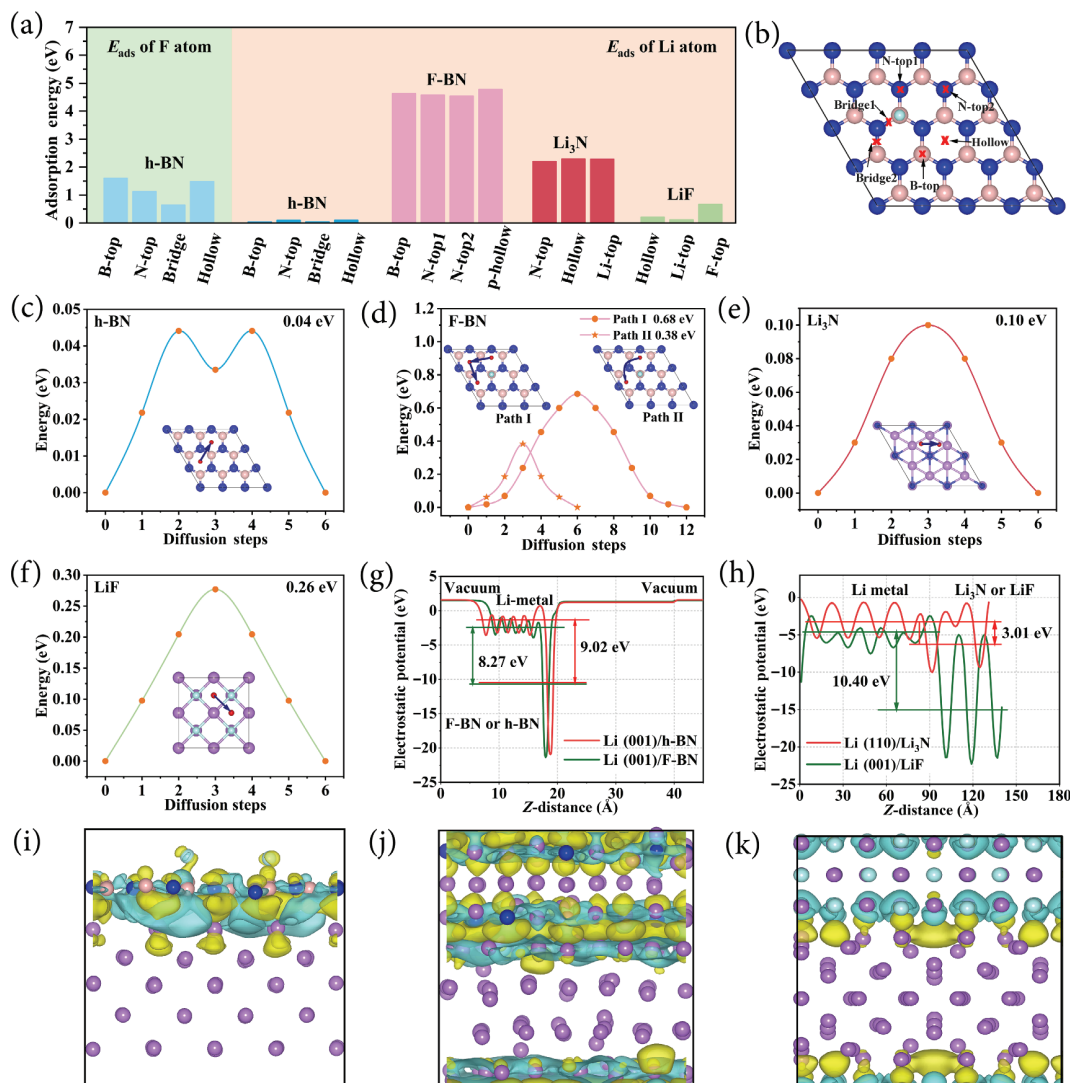


Figure 4 Mechanistic investigation into kinetics of Li plating. (a) Adsorption energies for F atom on h-BN when constructing F-BN model (green part) and for Li atom on h-BN, F-BN, Li_3N , and LiF (pink part). (b) The adsorption sites for Li atom on F-BN. (c)–(f) Migration paths and diffusion barriers of Li^+ on h-BN, F-BN, Li_3N , and LiF, respectively. (g) and (h) Electrostatic potential distribution at the interface of Li (001)/h-BN (001), Li (001)/F-BN (001), Li (110)/ Li_3N (001), and Li (001)/LiF (001), respectively. (i)–(k) Side-view of charge transfer of Li/F-BN, Li/ Li_3N , and Li/LiF, where the blue area means charge decrease and the yellow area means charge increase.

barrier is required to uniformize the distribution of lithium and avoid the accumulation of adsorbed lithium to evolve into dendrites [45]. Li-ions diffuse through Li–N and Li–F bridge sites on Li_3N (001) and LiF (001) surfaces, respectively. Li_3N (001) exhibits a lower Li-ion diffusion barrier of 0.10 eV compared with that of LiF (001) (0.26 eV). These results demonstrate that Li_3N as a favorable component in ASEI exhibits better lithiophilicity and lower ion diffusion barrier, which allow uniform Li deposition with a reduced nucleation overpotential.

The electrostatic potential distribution at the interface and supercell was investigated to analyze the electronic conductivity (Figs. 4(g) and 4(h)). Each valley of the curve represents the potential of the atomic layer at that location. The potential curve of the Li metal part oscillates in the high-potential region, while rapidly dropping to the low-potential region in the substrate or ASEI. Electrons tend to be transported from the Li side with smaller work function to the other side of the interface with larger work function. The internal electric field established by the macroscopic average potential differences on both sides can hinder electron tunneling. Both the interfaces of h-BN and F-BN have a huge electron tunneling barrier, with values of 9.02 and 8.27 eV, respectively, indicating that fluorination process does not have much effect on the insulating properties of BN. As a narrow

bandgap semiconductor (0.96 eV, Fig. S17(a) in the ESM), Li_3N forming interface with Li (110) has a lower electron tunneling barrier (3.01 eV). Whereas the bandgap of LiF is as high as 9.14 eV (Fig. S17(b) in the ESM), a higher barrier (10.4 eV) of LiF (001)/Li (001) interface was required to tunnel through the SEI. Therefore, LiF can function as an electronic insulator between electrode and electrolyte, reducing the possibility of dendrite growth.

We further investigated the interface properties between lithium and the four components. Considering the lattice matching, we selected the Li (001) surface to form the interfaces with h-BN, F-BN, and LiF, while the Li (110) surface to form the interface with Li_3N , which are the two low-index surfaces with the largest lithium exposure area [46]. The lattice mismatch of all constructed interfaces is less than 3%, the detailed supercell and geometrically optimized parameters are given in Tables S1 and S2 in the ESM. It can be found that both h-BN and F-BN are in good agreement with the lithium surface lattice (Figs. S18(a) and S18(b) in the ESM) and almost no geometric deformation occurs when the interface is formed, indicating that the fluorination process retains the high mechanical strength of BN. In addition, the interlayer spacing of F-BN/Li (001) is 2.29 Å, which is significantly lower than that of the h-BN/Li (001) interface (3.35 Å). The

corresponding interfaces of $\text{Li}_3\text{N}/\text{Li}$ (110) and LiF/Li (001) show a significant distortion after geometric optimization (Fig. S19 in the ESM). The binding interactions of the interface formed by the two substrates were compared, F-BN/Li (001) produces the larger adhesion energy and interfacial energy than h-BN/Li (001). The adhesion energy of the interface formed by Li_3N and lithium is calculated to be $0.58 \text{ J}\cdot\text{m}^{-2}$, which is higher than the minimum adhesion energy ($0.5 \text{ J}\cdot\text{m}^{-2}$) required for smooth and flat lithium deposition. The adhesion energy of the LiF/Li (001) interface is slightly smaller ($0.33 \text{ J}\cdot\text{m}^{-2}$), but its interfacial energy is $0.77 \text{ J}\cdot\text{m}^{-2}$, which is higher than the interfacial energy of $0.43 \text{ J}\cdot\text{m}^{-2}$ on the $\text{Li}_3\text{N}/\text{Li}$ (110) interface. A high adhesion energy can promote the uniform Li deposition by uniformizing the Li-ion concentration distribution and current density at the electrode/electrolyte interface, while a large interfacial energy represents the thermodynamic stability of the interface, so that the interface presents a low impedance [47, 48].

The charge density difference at the interface can reflect the charge interaction of substrates and lithium. As shown in Fig. S20 in the ESM and Fig. 4(i), only van der Waals force exists in h-BN/Li (001), thus the charge transfer is quite limited. However, the electronic structure of h-BN has been changed by the

introduction of fluorine atoms. The electronic interaction of F-BN/Li(001) interface becomes stronger, which is consistent with the increase in the adsorption energy of Li on the fluoridated substrate. In comparison, the charge transfer at the $\text{Li}_3\text{N}/\text{Li}$ (110) interface is dramatic, which is due to the half-filled N-2p orbital in the Li_3N electronic structure can accept a large number of electrons from the Li-bulk side (Fig. 4(j)). Moreover, Li_3N is stacked as a layered structure of Li_2N and Li^+ layers with weak geometric stability [49], thus showing a wider charge transfer region on the charge density difference map. In contrast, the electron redistribution at LiF (001)/Li (001) interface (Fig. 4(k)) is gentler, and the charge transfer only occurs near the interfacial region, indicating the better stability of LiF.

Based on the above discussion, it can be established that the key to determine Li deposition behavior is whether the substrate can stabilize lithium at the initial stage of deposition and whether the ASEI with effective regulation can be generated in subsequent cycles. Figures 5(a)–5(c) give detailed illustrations of Li deposition in three substrates. Due to the lithophobicity of Cu, lithium tends to nucleate unevenly. The as-formed natural SEI lacks the capability to regulate Li plating and its inhomogeneity continues to exacerbate, triggering the dendrite growth. The uncontrolled

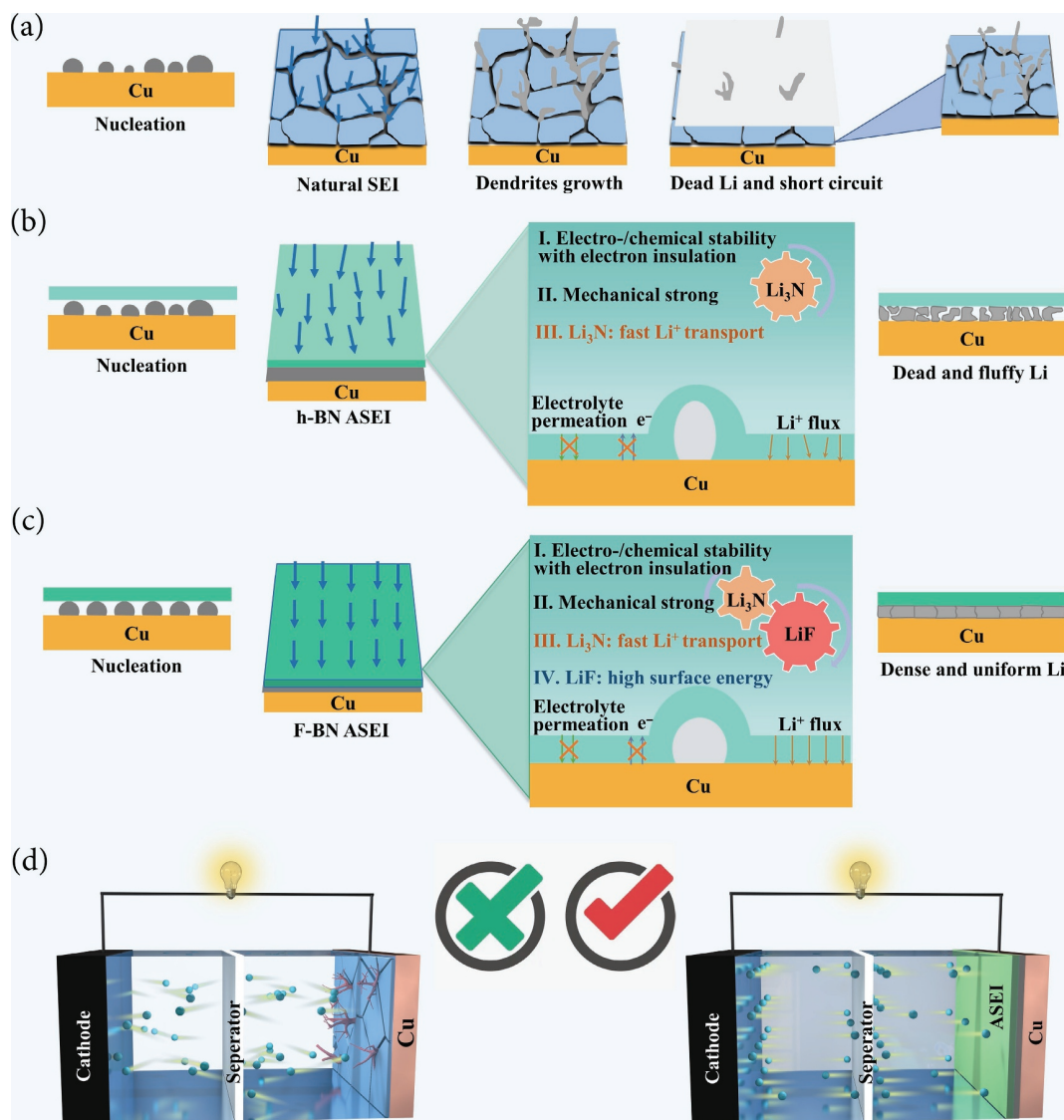


Figure 5 Schematic illustration of different Li plating process. (a) Unevenly Li nucleation develops into dendrites and destroys the fragile inherent SEI. The growing dendrites pierce the separator causing short circuit in the cell. (b) Li_3N in h-BN ASEI facilitates the fast Li^+ transport and has a certain regulating effect on the uniform deposition of lithium, but it is limited. The high mechanical strength of h-BN inhibits the growth of dendrites, and the electronic insulation hinders the decomposition of the electrolyte. (c) Under the synergistic effects of Li_3N with fast Li^+ transport and LiF with high interfacial energy, Li is uniformly and densely plated underneath the F-BN ASEI, and the close contact with the F-BN substrate ensures dendrite-free. (d) Diagram of internal operation in anode-free full cells with bare Cu and ASEI.

dendrites will permeate the separator and eventually lead to a short circuit. Although the Li_3N -containing ASEI generated in h-BN is indeed favorable for Li deposition, it cannot effectively combine with Li at the early stage of deposition due to the weak van der Waals force between h-BN and Li. Besides, the capability of Li_3N alone to adjust Li ions is limited, resulting in that the deposited Li is still relatively fluffy. However, the boron nitride becomes more lithiophilic after fluorination, which can anchor Li and *in-situ* formation of ASEI containing both LiF and Li_3N during cycling. The heterogeneous synergy of the electronically insulative LiF and the ion-conductive Li_3N results in a fast Li^+ transport through the ASEI layer, realizing dendrite-free Li deposition underneath the coating. Finally, the high stiffness of boron nitride also ensures that dendrite growth can be inhibited if occurs, prolonging the cycle life and safety of batteries.

To sum up, the synergistic effects of *in-situ* heterogeneous LiF and Li_3N interphases realize a dendrite-free Li deposition scenarios, resulting in a long-term cycling performance of anode-free full cells (Fig. 5(d)).

4 Conclusions

In conclusion, the lithiophilic fluorinated boron nitride exhibits the capability to improve the stability of Li plating and stripping due to the *in-situ* heterogeneous LiF and Li_3N interphases during cycling. The internal mechanism of interfacial synergy within the heterogeneous components has been well elucidated both theoretically and experimentally. These two beneficial components synergistically uniform Li distribution by modulating the electronic structure and ionic conductivity of the ASEI, achieving dense Li deposition. The electronically insulating LiF component prevents electrolyte decomposition caused by electron tunneling. Furthermore, the inherently high mechanical strength of boron nitride becomes the last insurance for dendrite-free growth. On the basis of such a feasible scheme of heterogeneous interphases, we further propose the critical factors affecting Li deposition, that is, whether the substrate can stabilize Li at the initial stage of deposition and whether the interphases with effective regulation capability can be generated in the subsequent cycles. The two promising components (LiF and Li_3N) also laid the foundation for the rational design of artificial interphases in lithium metal batteries.

Acknowledgements

The work is supported by the National Natural Science Foundation of China (Nos. 52003038 and 52192610), Startup funds of Yangtze Delta Region Institute (Huzhou), University of Electronic Science and Technology of China (No. U03210019).

References

- Qiao, Y.; Yang, H. J.; Chang, Z.; Deng, H.; Li, X.; Zhou, H. S. A high-energy-density and long-life initial-anode-free lithium battery enabled by a Li_2O sacrificial agent. *Nat. Energy* **2021**, *6*, 653–662.
- Lee, M. J.; Han, J.; Lee, K.; Lee, Y. J.; Kim, B. G.; Jung, K. N.; Kim, B. J.; Lee, S. W. Elastomeric electrolytes for high-energy solid-state lithium batteries. *Nature* **2022**, *601*, 217–222.
- Zhang, Z. W.; Li, Y. Z.; Xu, R.; Zhou, W. J.; Li, Y. B.; Oyakhire, S. T.; Wu, Y. C.; Xu, J. W.; Wang, H. S.; Yu, Z. A. et al. Capturing the swelling of solid–electrolyte interphase in lithium metal batteries. *Science* **2022**, *375*, 66–70.
- Hobold, G. M.; Lopez, J.; Guo, R.; Minafra, N.; Banerjee, A.; Meng, Y. S.; Shao-Horn, Y.; Gallant, B. M. Moving beyond 99.9% Coulombic efficiency for lithium anodes in liquid electrolytes. *Nat. Energy* **2021**, *6*, 951–960.
- Zhou, G. M.; Chen, H.; Cui, Y. Formulating energy density for designing practical lithium-sulfur batteries. *Nat. Energy* **2022**, *7*, 312–319.
- Hu, A. J.; Chen, W.; Du, X. C.; Hu, Y.; Lei, T. Y.; Wang, H. B.; Xue, L. X.; Li, Y. Y.; Sun, H.; Yan, Y. C. et al. An artificial hybrid interphase for an ultrahigh-rate and practical lithium metal anode. *Energy Environ. Sci.* **2021**, *14*, 4115–4124.
- Wu, H.; Yao, Z. G.; Wu, Q. P.; Fan, S. S.; Yin, C. L.; Li, C. L. Confinement effect and air tolerance of Li plating by lithiophilic poly(vinyl alcohol) coating for dendrite-free Li metal batteries. *J. Mater. Chem. A* **2019**, *7*, 22257–22264.
- Niu, C. J.; Liu, D. Y.; Lochala, J. A.; Anderson, C. S.; Cao, X.; Gross, M. E.; Xu, W.; Zhang, J. G.; Whittingham, M. S.; Xiao, J. et al. Balancing interfacial reactions to achieve long cycle life in high-energy lithium metal batteries. *Nat. Energy* **2021**, *6*, 723–732.
- Paul, P. P.; McShane, E. J.; Colclasure, A. M.; Balsara, N.; Brown, D. E.; Cao, C. T.; Chen, B. R.; Chinnam, P. R.; Cui, Y.; Dufek, E. J. et al. A review of existing and emerging methods for lithium detection and characterization in Li-ion and Li-metal batteries. *Adv. Energy Mater.* **2021**, *11*, 2100372.
- Boyle, D. T.; Huang, W.; Wang, H.; Li, Y.; Chen, H.; Yu, Z.; Zhang, W.; Bao, Z.; Cui, Y. Corrosion of lithium metal anodes during calendar ageing and its microscopic origins. *Nat. Energy* **2021**, *6*, 487–494.
- Fedorov, R. G.; Maletti, S.; Heubner, C.; Michaelis, A.; Ein-Eli, Y. Molecular engineering approaches to fabricate artificial solid–electrolyte interphases on anodes for Li-ion batteries: A critical review. *Adv. Energy Mater.* **2021**, *11*, 2101173.
- Hu, Z. L.; Wang, C.; Wang, C.; Chen, B. B.; Yang, C. P.; Dong, S. M.; Cui, G. L. Uncovering the critical impact of the solid electrolyte interphase structure on the interfacial stability. *InfoMat* **2022**, *4*, e12249.
- Liu, Y. H.; Sun, J. M.; Hu, X. Q.; Li, Y. F.; Du, H. F.; Wang, K.; Du, Z. Z.; Gong, X.; Ai, W.; Huang, W. Lithiophilic sites dependency of lithium deposition in Li metal host anodes. *Nano Energy* **2022**, *94*, 106883.
- Wu, H. P.; Jia, H.; Wang, C. M.; Zhang, J. G.; Xu, W. Recent progress in understanding solid electrolyte interphase on lithium metal anodes. *Adv. Energy Mater.* **2021**, *11*, 2003092.
- Liu, Y. J.; Tao, X. Y.; Wang, Y.; Jiang, C.; Ma, C.; Sheng, O. W.; Lu, G. X.; Lou, X. W. Self-assembled monolayers direct a LiF-rich interphase toward long-life lithium metal batteries. *Science* **2022**, *375*, 739–745.
- Chen, M.; Zheng, J. H.; Liu, Y. J.; Sheng, O. W.; Ju, Z. J.; Lu, G. X.; Liu, T. F.; Wang, Y.; Nai, J. W.; Wang, Q. et al. Marrying ester group with lithium salt: Cellulose-acetate-enabled LiF-enriched interface for stable lithium metal anodes. *Adv. Funct. Mater.* **2021**, *31*, 2102228.
- Chen, J.; Fan, X. L.; Li, Q.; Yang, H. B.; Khoshi, M. R.; Xu, Y. B.; Hwang, S.; Chen, L.; Ji, X.; Yang, C. Y. et al. Electrolyte design for LiF-rich solid–electrolyte interfaces to enable high-performance micro-sized alloy anodes for batteries. *Nat. Energy* **2020**, *5*, 386–397.
- Fan, X. L.; Ji, X.; Han, F. D.; Yue, J.; Chen, J.; Chen, L.; Deng, T.; Jiang, J. J.; Wang, C. S. Fluorinated solid electrolyte interphase enables highly reversible solid-state Li metal battery. *Sci. Adv.* **2018**, *4*, eaau9245.
- Ma, X. X.; Shen, X.; Chen, X.; Fu, Z. H.; Yao, N.; Zhang, R.; Zhang, Q. The origin of fast lithium-ion transport in the inorganic solid electrolyte interphase on lithium metal anodes. *Small Struct.* **2022**, *3*, 2200071.
- Zhang, Q. K.; Liu, S.; Lu, Y. T.; Xing, L. D.; Li, W. S. Artificial interphases enable dendrite-free Li-metal anodes. *J. Energy Chem.* **2021**, *58*, 198–206.
- Zhao, Q.; Stalin, S.; Archer, L. A. Stabilizing metal battery anodes through the design of solid electrolyte interphases. *Joule* **2021**, *5*, 1119–1142.
- Ye, S. F.; Wang, L. F.; Liu, F. F.; Shi, P. C.; Wang, H. Y.; Wu, X. J.; Yu, Y. $\text{g-C}_3\text{N}_4$ derivative artificial organic/inorganic composite solid electrolyte interphase layer for stable lithium metal anode. *Adv. Energy Mater.* **2020**, *10*, 2002647.
- Tan, J.; Matz, J.; Dong, P.; Shen, J. F.; Ye, M. X. A growing appreciation for the role of LiF in the solid electrolyte interphase. *Adv. Energy Mater.* **2021**, *11*, 2100046.
- Su, H.; Liu, Y.; Zhong, Y.; Li, J. R.; Wang, X. L.; Xia, X. H.; Gu, C.

- D.; Tu, J. P. Stabilizing the interphase between Li and argyrodite electrolyte through synergistic phosphating process for all-solid-state lithium batteries. *Nano Energy* **2022**, *96*, 107104.
- [25] Kresse, G.; Furthmüller, J. Efficient iterative schemes for *ab initio* total-energy calculations using a plane-wave basis set. *Phys. Rev. B* **1996**, *54*, 11169–11186.
- [26] Perdew, J. P.; Chevary, J. A.; Vosko, S. H.; Jackson, K. A.; Pederson, M. R.; Singh, D. J.; Fiolhais, C. Erratum: Atoms, molecules, solids, and surfaces: Applications of the generalized gradient approximation for exchange and correlation. *Phys. Rev. B* **1993**, *48*, 4978.
- [27] Blöchl, P. E. Projector augmented-wave method. *Phys. Rev. B* **1994**, *50*, 17953–17979.
- [28] Henkelman, G.; Uberuaga, B. P.; Jónsson, H. A climbing image nudged elastic band method for finding saddle points and minimum energy paths. *J. Chem. Phys.* **2000**, *113*, 9901–9904.
- [29] Venkateswarlu, G.; Madhu, D.; Rani, J. V. An effective performance of F-doped hexagonal boron nitride nanosheets as cathode material in magnesium battery. *Mater. Chem. Phys.* **2019**, *226*, 356–361.
- [30] Bai, Y. Q.; Zhang, J.; Wang, Y. F.; Cao, Z. Y.; An, L. L.; Zhang, B.; Yu, Y. L.; Zhang, J. Y.; Wang, C. M. Ball milling of hexagonal boron nitride microflakes in ammonia fluoride solution gives fluorinated nanosheets that serve as effective water-dispersible lubricant additives. *ACS Appl. Nano Mater.* **2019**, *2*, 3187–3195.
- [31] Radhakrishnan, S.; Das, D.; Samanta, A.; de los Reyes, C. A.; Deng, L. Z.; Alemany, L. B.; Weldeghiorghis, T. K.; Khabashesku, V. N.; Kochat, V.; Jin, Z. H. et al. Fluorinated h-BN as a magnetic semiconductor. *Sci. Adv.* **2017**, *3*, e1700842.
- [32] Zeng, X. H.; Xie, K. X.; Liu, S. L.; Zhang, S. L.; Hao, J. N.; Liu, J. T.; Pang, W. K.; Liu, J. W.; Rao, P. H.; Wang, Q. H. et al. Bio-inspired design of an *in situ* multifunctional polymeric solid-electrolyte interphase for Zn metal anode cycling at 30 mA·cm⁻² and 30 mAh·cm⁻². *Energy Environ. Sci.* **2021**, *14*, 5947–5957.
- [33] Liu, Y. X.; Hu, R. Z.; Zhang, D. C.; Liu, J. W.; Liu, F.; Cui, J.; Lin, Z. P.; Wu, J. S.; Zhu, M. Constructing Li-rich artificial SEI layer in alloy-polymer composite electrolyte to achieve high ionic conductivity for all-solid-state lithium metal batteries. *Adv. Mater.* **2021**, *33*, 2004711.
- [34] Han, F. D.; Westover, A. S.; Yue, J.; Fan, X. L.; Wang, F.; Chi, M. F.; Leonard, D. N.; Dudney, N. J.; Wang, H.; Wang, C. S. High electronic conductivity as the origin of lithium dendrite formation within solid electrolytes. *Nat. Energy* **2019**, *4*, 187–196.
- [35] Yao, Y. X.; Zhang, X. Q.; Li, B. Q.; Yan, C.; Chen, P. Y.; Huang, J. Q.; Zhang, Q. A compact inorganic layer for robust anode protection in lithium-sulfur batteries. *InfoMat* **2020**, *2*, 379–388.
- [36] Pathak, R.; Chen, K.; Gurung, A.; Reza, K. M.; Bahrami, B.; Pokharel, J.; Baniya, A.; He, W.; Wu, F.; Zhou, Y. et al. Fluorinated hybrid solid-electrolyte-interphase for dendrite-free lithium deposition. *Nat. Commun.* **2020**, *11*, 93.
- [37] Nanda, S.; Manthiram, A. Delineating the lithium–electrolyte interfacial chemistry and the dynamics of lithium deposition in lithium-sulfur batteries. *Adv. Energy Mater.* **2021**, *11*, 2003293.
- [38] Cheng, H.; Gao, C.; Cai, N.; Wang, M. Ag coated 3D-Cu foam as a lithiophilic current collector for enabling Li₂S-based anode-free batteries. *Chem. Commun.* **2021**, *57*, 3708–3711.
- [39] Nanda, S.; Bhargava, A.; Jiang, Z.; Zhao, X. H.; Liu, Y. Y.; Manthiram, A. Implications of *in situ* chalcogen substitutions in polysulfides for rechargeable batteries. *Energy Environ. Sci.* **2021**, *14*, 5423–5432.
- [40] Sun, J. M.; Liu, Y. H.; Liu, L.; He, S.; Du, Z. Z.; Wang, K.; Xie, L. H.; Du, H. F.; Ai, W. Expediting sulfur reduction/evolution reactions with integrated electrocatalytic network: A comprehensive kinetic map. *Nano Lett.* **2022**, *22*, 3728–3736.
- [41] Wang, G. Y.; Zhu, M.; Zhang, Y.; Song, C.; Zhu, X. L.; Huang, Z. Y.; Zhang, Y. J.; Yu, F. F.; Xu, G.; Wu, M. H. et al. Double interface regulation: Toward highly stable lithium metal anode with high utilization. *InfoMat* **2022**, *4*, e12293.
- [42] Han, F. D.; Yue, J.; Fan, X. L.; Gao, T.; Luo, C.; Ma, Z. H.; Suo, L. M.; Wang, C. S. High-performance all-solid-state lithium-sulfur battery enabled by a mixed-conductive Li₂S nanocomposite. *Nano Lett.* **2016**, *16*, 4521–4527.
- [43] Tan, G. Q.; Xu, R.; Xing, Z. Y.; Yuan, Y. F.; Lu, J.; Wen, J. G.; Liu, C.; Ma, L.; Zhan, C.; Liu, Q. et al. Burning lithium in CS₂ for high-performing compact Li₂S-graphene nanocapsules for Li-S batteries. *Nat. Energy* **2017**, *2*, 17090.
- [44] Zhang, R.; Chen, X. R.; Chen, X.; Cheng, X. B.; Zhang, X. Q.; Yan, C.; Zhang, Q. Lithiophilic sites in doped graphene guide uniform lithium nucleation for dendrite-free lithium metal anodes. *Angew. Chem., Int. Ed.* **2017**, *56*, 7764–7768.
- [45] Jäckle, M.; Groß, A. Microscopic properties of lithium, sodium, and magnesium battery anode materials related to possible dendrite growth. *J. Chem. Phys.* **2014**, *141*, 174710.
- [46] Shi, L.; Xu, A.; Zhao, T. S. First-principles investigations of the working mechanism of 2D h-BN as an interfacial layer for the anode of lithium metal batteries. *ACS Appl. Mater. Interfaces* **2017**, *9*, 1987–1994.
- [47] Xu, B. Q.; Liu, Z.; Li, J. X.; Huang, X.; Qie, B. Y.; Gong, T. Y.; Tan, L. Y.; Yang, X. J.; Paley, D.; Dontigny, M. et al. Engineering interfacial adhesion for high-performance lithium metal anode. *Nano Energy* **2020**, *67*, 104242.
- [48] Zhu, J. G.; Li, P. K.; Chen, X.; Legut, D.; Fan, Y. C.; Zhang, R. F.; Lu, Y. Y.; Cheng, X. B.; Zhang, Q. F. Rational design of graphitic–inorganic Bi-layer artificial SEI for stable lithium metal anode. *Energy Storage Mater.* **2019**, *16*, 426–433.
- [49] Alpen, U. V.; Rabenau, A.; Talat, G. H. Ionic conductivity in Li₃N single crystals. *Appl. Phys. Lett.* **1977**, *30*, 621–623.